

Experimental study on orientation and de-mixing phenomena of elongated particles in gas-fluidized beds



L. Boer ^a, K.A. Buist ^{b,*}, N.G. Deen ^c, J.T. Padding ^d, J.A.M. Kuipers ^b

^a Interfaces With Mass Transfer, Department of Chemical Engineering & Chemistry, Eindhoven University of Technology, P.O. box 513, 5600 MB Eindhoven, The Netherlands

^b Multiphase Reactors Group, Department of Chemical Engineering & Chemistry, Eindhoven University of Technology, P.O. box 513, 5600 MB Eindhoven, The Netherlands

^c Multiphase & Reactive Flows Group, Department of Mechanical Engineering, Eindhoven University of Technology, P.O. box 513, 5600 MB Eindhoven, The Netherlands

^d Intensified Reaction and Separation Systems Group, Process & Energy Department, Delft University of Technology, Leeghwaterstraat 39, 2628 CB Delft, The Netherlands

ARTICLE INFO

Article history:

Received 17 May 2017

Received in revised form 26 January 2018

Accepted 30 January 2018

Available online 4 February 2018

Keywords:

Fluidized beds

Fluidization

Mixing

Segregation

Granular dynamics

Particle shape

ABSTRACT

In this experimental study the segregation behavior for fluidized mixtures of spherical and cylindrical particles is investigated. In industry, fluidization of particles featuring a wide range of shapes is common in various applications such as biomass gasification, drying applications, food processing and production of pharmaceuticals. Earlier publications have mainly focused on segregation of spherical particles of different volume or density. The particles used in this study have equal volume and density but a different shape. The main purpose of this work is to study de-mixing driven by particle shape.

To analyze the particle distributions inside the fluidized bed, a Digital Image Analysis (DIA) technique has been developed, capable of capturing the particle positions and orientations within the bed over time. The experiments show that in the non-bubbling flow regime (at low fluidization velocities) rod-shaped particles may segregate, sinking to the bottom of the bed. In the bubbling flow regime (at higher fluidization velocities) segregation does not occur, because of bubble-induced mixing. Here strong alignment of the cylindrical particle's long axis with the flow is observed. The experimental results obtained give qualitative and quantitative insight in the behavior of non-spherical particles in fluidized beds and can be used for validation of numerical models concerning non-spherical particle mixing.

© 2018 The Authors. Published by Elsevier B.V. This is an open access article under the CC BY-NC-ND license (<http://creativecommons.org/licenses/by-nc-nd/4.0/>).

1. Introduction

Ideal particulate systems consisting of mono-sized particles of equal densities seldom occur in practical fluidized bed applications. Instead, in practical applications particles of a wide size distribution and/or different densities are used. In these non-ideal systems, particle mixing and segregation can occur at specific operating conditions. A bed may be 'well fluidized' in the sense that all the particles are fully supported by the gas, but may still be segregated in the sense that the local bed composition does not correspond to the average [1]. Segregation is likely to occur when there is a substantial difference in the drag force per unit mass between different particles.

In this paper, segregation induced by differences in particle shape is examined. Most of the research reported so far focuses on segregation of spherical particles ([2–11]). The effect of particle size and density on segregation behavior has been documented [1,12] and is understood quite well in a qualitative sense. But non-spherical particles are often encountered in fluidized process equipment. An important example is the production of syngas from biomass in fluidized bed gasifiers. The

used bio-materials are typically milled before being fed to the gasifier, resulting in particles with common aspect ratios of 3 to 5, sometimes up to 12 [13]. The expected segregation behavior of such elongated particles is quite different from that of spheres [14]. Vollmari et al. [15] investigated mixing of bi-disperse systems of various particle shapes (spheres, cubes and plates) and showed that particle shape plays an important role in the mixing process. For elongated particles the projected area of a particle changes with orientation, and particles tend to align with the walls of the bed, leading to very different mixing dynamics [16]. The aforementioned studies analyzed mixing of an initially completely segregated system. In this work the opposite problem is studied; we will analyze segregation behavior in a fluidized bed starting from a well-mixed state. We will limit our studies to mixtures of spheres and rods of equal volume and density.

Mixing studies in fluidized beds require information on the transient particle positions in the bed. Several experimental techniques are available to measure the position and orientation of non-spherical particles, such as Position Emission Particle Tracking (PEPT) [17], Particle Tracking Velocimetry (PTV) [18], and Magnetic Particle Tracking (MPT) [19,20]. So far, these techniques were only used to study the orientation of individual particles. This requires long measurement times to obtain statistically significant data for the entire bed. Also, to

* Corresponding author.

E-mail address: K.A.Buist@tue.nl (K.A. Buist).

our knowledge, the co-alignment of particles has not been addressed yet. Particle tracking techniques are not capable of measuring this feature because only one particle is tracked. Using imaging techniques, such as Digital Image Analysis (DIA), it is possible to study the position and orientation of multiple particles simultaneously. The technique developed in this work builds on a technique developed by Olaofe et al. [21,22], but has now been extended to elongated particle shapes. Because the technique is intrinsically 2D, only the position and orientation of cylinders that are in plane with the front wall of the fluidized bed can be determined.

The outline of this paper is as follows. First the experimental methods and image analysis techniques are discussed in Sections 2 and 3 respectively. Section 4 deals with the basic theory on quantification of mixing phenomena. In Section 5 the experimental results are discussed. Finally, we present the main conclusions in Section 6.

2. Materials and methods

2.1. Materials

For the experiments, a shallow pseudo-2D fluidized bed was used, with dimensions listed in Table 1. The depth of the bed is approximately 5 particle diameters, which increases the visibility of the particles. Air is supplied to the bed by three tubes and redistributed evenly by a sintered metal porous plate at the bottom of the bed (see Fig. 1). The air supply is regulated by a mass flow controller, coupled to a PC. The maximum airflow is 630 NL/min, which corresponds to a superficial velocity of 8 m/s. Near the distributor plate a digital pressure sensor was mounted to dynamically measure the pressure drop over the bed.

The bed material consisted of stainless steel spheres and cylinders, mixed in various ratios. For visualization purposes some of the particles were painted (as seen in Fig. 1), but most of the experiments were performed using untreated particles featuring a bare metallic surface. Care was taken to give both particle species equal mass and volume but a different shape, since the subject of this study is shape-driven segregation.

The motion of the solid particles in the bed was captured by a 3-CCD camera (model JAI AT-200 GE) at a resolution of 1624×1236 pixels with a magnification of 7.8, yielding $90 \mu\text{m}/\text{pixel}$. Consequently, the spheres are recorded with a resolution of 30 pixels across the diameter and the cylinders are recorded with about 130 pixels along the length. A short shutter time combined with a relatively large aperture was used, yielding images with little motion blur, even at high particle velocities. Appropriate lighting is provided by two LED arrays, each consisting of 72 LED's giving 250 W of illumination per array.

3. Digital Image Analysis techniques

Digital Image Analysis (DIA) is used to analyze the images that were recorded during the experiments. The composition of the fluidized bed and the orientation of the cylindrical particles were determined using several image analysis techniques.

3.1. Determining bed composition

The spherical particles used in this research have a metallic finish and show distinguishable reflection spots when illuminated by a strong light (see Fig. 2a). Since the bed is illuminated by two LED light sources, each spherical particle -in principle- yields two reflections that can be clearly identified from the images. The cylindrical particles, on the other hand, have a rather dull surface that reflects light in a much more scattered way; no clearly defined reflection spot is observed. This difference in reflective properties between the particle species has been exploited to identify the two different particles species and subsequently determine the bed composition.

Table 1
Dimensions and properties of the fluidized bed and particles.

Vessel dimensions	$500 \times 100 \times 15$ mm (height, width, depth)
Bed material	0.5 kg stainless steel particles, ± 100 mm bed height
Spherical particle diameter	3 mm
Cylindrical particle diameter \times length	1.2×12 mm
Minimum fluidization velocity (spheres)	3.15 m/s

For the analysis, first the image is cropped, removing the side walls of the fluidized bed (Fig. 2a). Secondly the fraction of the image occupied by the solid phase is determined (see Fig. 2b). Since the particles and the background have a distinctly different color, this could be determined with relative ease. In the third step the DIA script counts the number of reflection spots in each grid cell (Fig. 2c, d). This is done using a circular Hough transform, available in MATLAB as the function imfindcircles. For the analysis of mixing the bed is divided into grid cells. For each cell the occupancy (2d solid volume fraction) and the number of reflections per unit of solids area can be computed (see Fig. 2e, f).

Finally, calibration was used to relate the number of reflections in each grid cell to the actual composition in that grid cell. In this way the number of reflections per grid cell N_r is obtained from the images, which can directly be used as a measure for the bed composition.

$$r = \frac{N_r}{A_{grid} \times \varepsilon_{solid}^{2D}} \quad (1)$$

The area of each grid cell occupied by the solid phase equals $A_{grid} \times \varepsilon_{solid}^{2D}$, where A_{grid} is the area of the grid cell, and ε_{solid}^{2D} is the fraction of the cell occupied by solid particles (in 2D). To obtain the number of reflections per unit of solid area (r), the number of reflections (N_r) is divided by the area occupied by the solid phase.

The maximum number of reflections one may encounter for a given grid size is obtained when spherical particles are packed in the most dense state possible. For circles in the 2D plane, this corresponds to a hexagonal packing, where the maximum number of reflections equals:

$$r_{max} = \frac{4}{\sqrt{3}d_p^2} \quad (2)$$

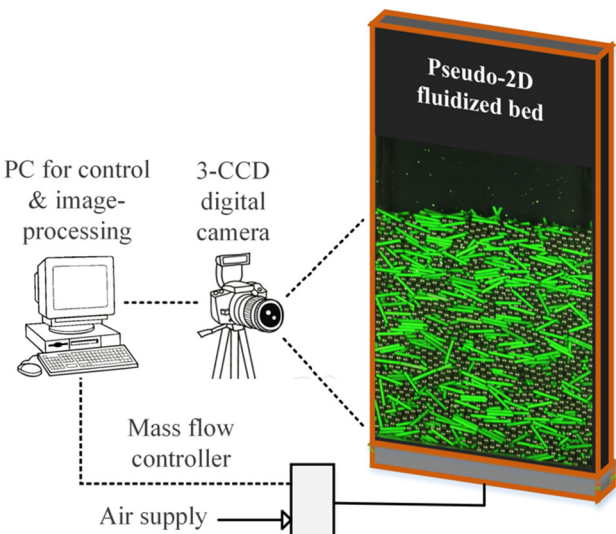


Fig. 1. Schematic of the experimental setup.

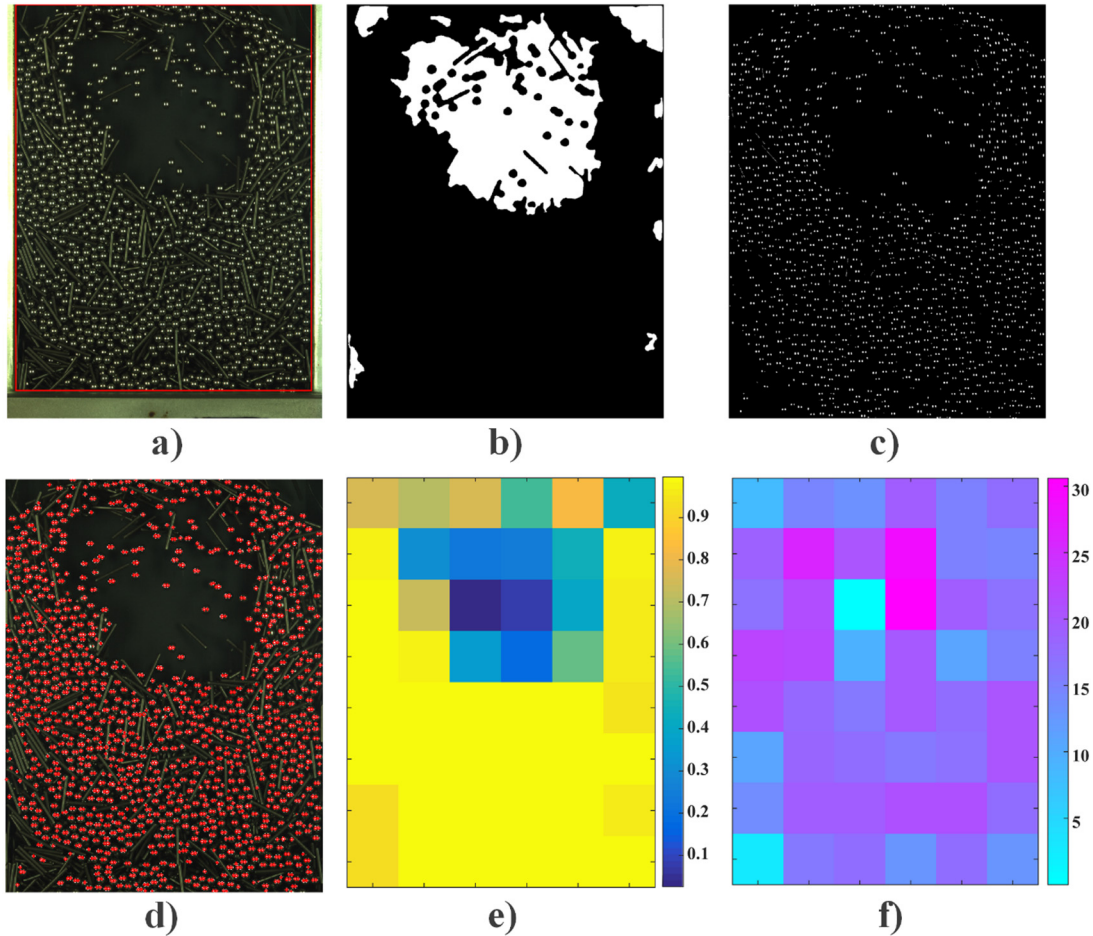


Fig. 2. Image processing steps for deriving mixing information. a) Raw image of fluidized bed filled with spherical and cylindrical particles, b) Distinction of solids phase from the background, c) Visualization of the reflection spots on spherical particles, d) Detected spherical particles, e) 2D solids volume fraction (ε_{solid}^{2D}), f) number of reflections per unit solids area (r).

where d_p is the particle diameter. In order to normalize our measurements, the obtained number of reflections per grid cell (r) is divided by the maximum possible (r_{max}), yielding:

$$|r| = \frac{\sqrt{3}d_p^2}{4} r \quad (3)$$

By calibration the normalized reflection count ($|r|$) was related to the volumetric bed composition (fraction of cylindrical particles) f . This calibration is required, because the number of visible particles in the 2D plane (which is proportional to $|r|$) is not equal to the volumetric-averaged composition (f). Therefore an empirical correlation between these quantities was derived [20,21].

The calibration was performed by fluidizing the bed at high gas velocities, such that the spherical and cylindrical particles remain well mixed. In that case the composition of each grid cell is equal to the average composition and calibration is straightforward. Mixtures containing a high fraction of cylindrical particles were difficult to fluidize in a homogenous fashion. Therefore these mixtures were pre-mixed by hand and poured into the fluidized bed manually. Calibration yielded the following relationship between the normalized reflection count ($|r|$) and the fraction of cylindrical particles (f):

$$(1-f) = 1.459|r|^3 - 0.459 |r| \quad (4)$$

The calibration curve is shown in Fig. 3. For convenience the regression model was expressed in terms of $(1-f)$, this sets the intercept to zero, reducing the degrees of freedom in the regression model.

The accuracy of the aforementioned calibration procedure was validated by imaging fluidizing beds of a known composition f , and processing the images using Eq. (4). Ideally the a priori known overall

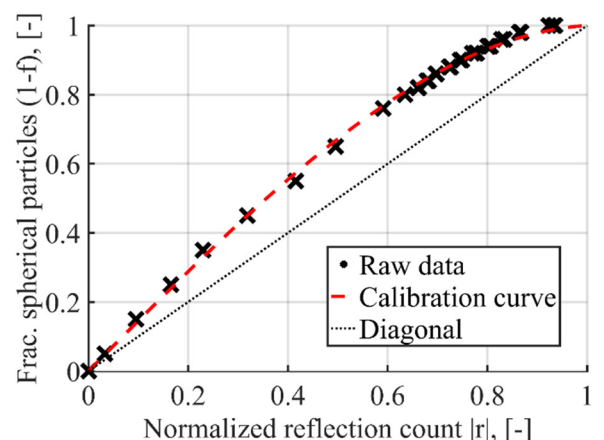


Fig. 3. Calibration curve, relating the amount of reflections per grid cell to the composition of the bed.

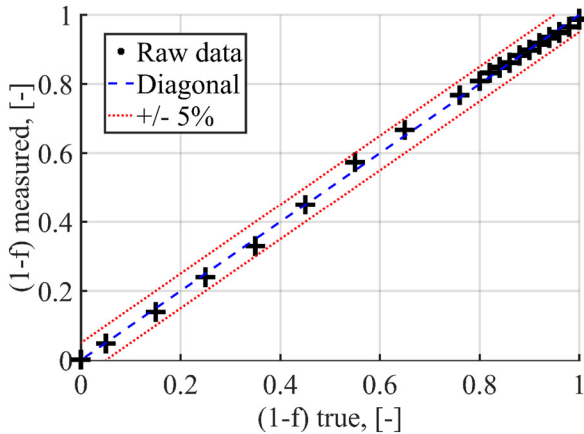


Fig. 4. Parity plot showing the relationship between the measured mass fraction and the true mass fraction, determined gravimetrically.

bed composition should be equal to the one measured by the DIA technique. Fig. 4 shows a parity plot of the overall bed composition actually used in the experiments, compared to that measured by the DIA technique. As can be seen there is good agreement between the measured values and the true conditions, making the DIA technique valid for determining volumetric-averaged compositions.

3.2. Determining cylinder orientation

The orientation of the cylindrical particles was determined using a linear Hough transform [23]. First the original RGB image is converted to HSV. The value of the image (V) now reveals the pixels that have

the highest intensity gradient. Secondly, all the small objects in the image are removed, that relate to the spherical particles. Thirdly, any remaining artifacts are enhanced by thickening the edges. After these three steps the cylindrical particles are clearly visible (see Fig. 5b). Now the image is processed in MATLAB using the Hough routine, identifying the position and orientation of the cylindrical particles (Fig. 5c).

The Hough procedure is intended to detect objects of a size with the same order-of-magnitude as the image size. To meet this criterion, the image plane was divided into grid cells, performing the Hough routine on each grid cell separately. A second iteration was performed on a different grid to make sure also cylinders laying on the intersection of two grid cells were detected properly. To prevent double detection in the second iteration, all cylinders detected in the first iteration were removed from the image. This was done by applying a mask (Fig. 5d, e). After applying the mask the remaining particles are analyzed again on a different grid, revealing the undetected particles (Fig. 5f).

Compared to the total number of particles in the bed, only a few cylinders are visible in each image (typically 8–11%). Most particles are not detected because a) they are not located near the front wall, b) they are obstructed by other particles or c) they are strongly inclined towards the z-direction, reducing their projected area in the xy-plane. The relatively low total recovery is not related to the specific method, but can be considered as an intrinsic feature of 2D imaging techniques.

Nonetheless, most of the particles close to the front wall could be detected. Verification of the image processing routine showed that the orientation of most visible particles is detected (86–92%). It was observed that the remaining undetected particles were not biased towards a certain orientation. This means that the sample taken is statistically representative for the entire population.

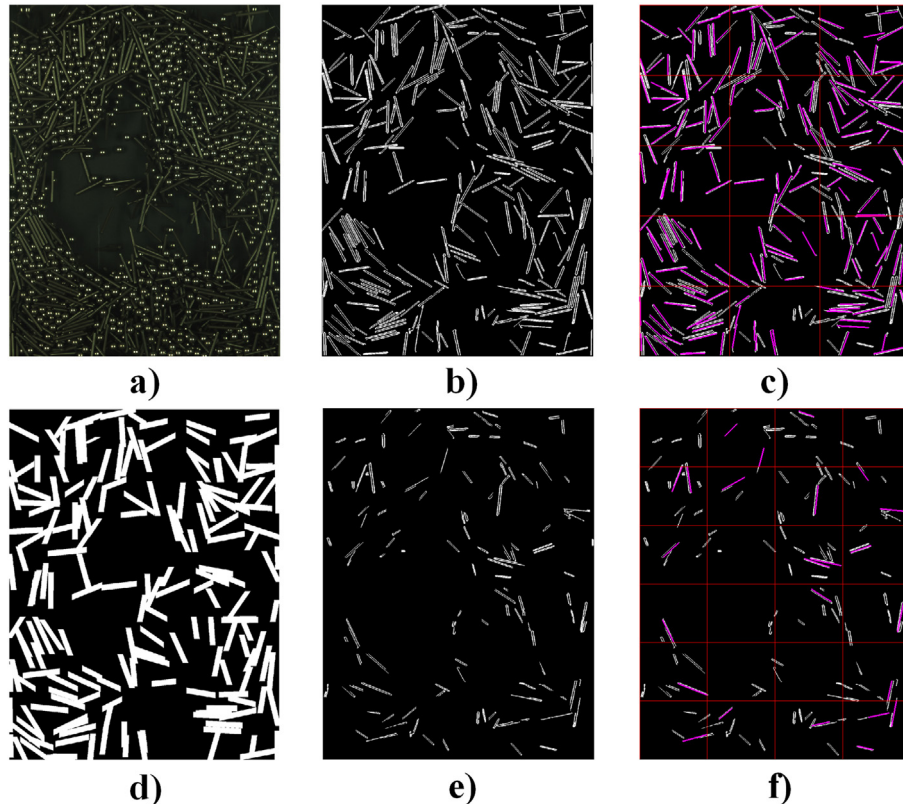


Fig. 5. Image processing steps for deriving the orientation of cylindrical particles. a) original image, b) edge detection + removal of small objects, c) detected lines from first iteration, d) image mask of detected lines, e) edge detection – mask, f) lines detection on 2nd grid.

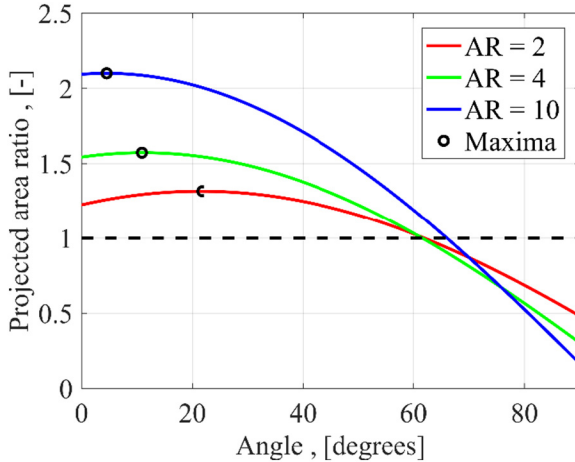


Fig. 6. Projected area ratio of cylindrical particles of aspect ratio AR, compared to a volume-equivalent sphere as a function of inclination angle (see Eq. (10)).

4. Theory

4.1. Characterizing the degree of mixing

To characterize mixing in a bed of solid particles, several methods have been published [24]. Most of these methods are only applicable to simulations, because they require details on the exact position of each particle over time. This information is not obtained easily by experiments, due to practical limitations. A mixing characteristic applicable to both experimental and simulation data is the Lacey mixing index [24].

For a fluidized bed filled with a binary mixture of species i and j , the concentration of species i is defined as f_i , and $f_i + f_j = 1$. When the total bed is divided into N grid cells (either 2D or 3D), the mixing variance S^2 is defined as:

$$S^2 = \frac{1}{N-1} \sum_{k=1}^N (f_i^k - \langle f \rangle)^2 \quad (5)$$

where N is the number of cells in the bed, f_i^k is the fraction of particle species i in cell k and $\langle f \rangle$ is the bed-average concentration. The variance of the unmixed (i.e. completely segregated) bed equals:

$$S_{UM}^2 = \langle f \rangle - \langle f \rangle^2 \quad (6)$$

For an ideally mixed bed, the variance is equal to:

$$S_M^2 = \frac{S_{UM}^2}{n} \quad (7)$$

Here n is the average number of particles per cell. Now the dimensionless mixing index M , ranging from 0 to 1; from complete segregation to ideal mixing, can be expressed as:

$$M = \frac{S^2 - S_{UM}^2}{S_M^2 - S_{UM}^2} \quad (8)$$

Due to the use of grid cells the Lacey mixing index is grid dependent. A coarse grid gives higher mixing indices, since in that case the micro mixing effects are neglected. A fine grid gives lower mixing indices, if only a few particles are present per cell. When only one particle is present per cell, the Lacey index always considers the system to be fully segregated [25]. Therefore, the grid size should be chosen with care to obtain sensible results. For our system we chose to use a 5×7 grid (width, height). The grid size is then approximately 6 times the spherical particle's diameter, which allows for a maximum of 40 spheres

per grid cell. This grid size yields sufficient particle counts without over-averaging.

4.2. Comparison of the drag force on cylindrical and spherical particles

In this paper the segregation behavior for mixtures of spherical and cylindrical particles of equal volume and mass is investigated. Since all particles have the same mass, the gravity force on both particle species is equal. Therefore the driving force for segregation must be related to differences in the other dominant force exerted on the particles: the drag force induced by the gas. If, for now, we assume that the drag force coefficient (C_d) is constant irrespective of the particle's orientation, then the drag force scales linear with the particle's projected area.

For volume-equivalent spherical and cylindrical particles, the dimensions of the particles are related by $V = \frac{\pi}{6} d_s^3 = \frac{\pi}{4} d_c^3 AR$. Here d_s and d_c are the diameters of the spherical and cylindrical particles and AR is the aspect ratio of the cylinder. One can express d_c in terms of the other variables as $d_c = (\frac{2}{3AR})^{\frac{1}{3}} d_s$.

The projected area of a cylinder with aspect ratio AR for any inclination angle θ equals:

$$PA_c(\theta) = \left(\frac{2}{3AR} \right)^{\frac{2}{3}} d_s^2 (AR \cos(\theta) + \frac{\pi}{4} \sin(\theta)) \quad (9)$$

Here θ is the inclination angle ranging from [0,90] degrees, where 0 corresponds to the flat/horizontal position and 90 corresponds to the vertical/standing position. Now, taking the ratio of the projected areas of a cylinder and a sphere, we obtain:

$$PA_{ratio}(\theta) = \frac{PA_c}{PA_s} = \left(\frac{2}{3AR} \right)^{\frac{2}{3}} \left(\frac{4AR \cos(\theta)}{\pi} + \sin(\theta) \right) \quad (10)$$

The result is plotted for three different aspect ratios in Fig. 6, where $AR = 10$ corresponds to the particles used in our experiments. As can be seen, the projected ratio exceeds unity for $\theta < 60^\circ$ and decreases strongly upon approaching the vertical orientation ($\theta = 90$). As AR increases, the effect of the inclination angle becomes stronger.

Since the orientation of the particle in the bed is a priori unknown, one could estimate the drag force ratio acting on both particle species, based on the average orientation. If a cylindrical particle is only allowed to rotate in the xy-plane, then each inclination angle θ is equally probable. In that case the θ -averaged projected area ratio, denoted as $\overline{PA}_{ratio}(2D)$, can be found by integrating Eq. (10), yielding:

$$\overline{PA}_{ratio}(2D) = \frac{2}{\pi} \int_0^{\pi/2} PA_{ratio}(\theta) d\theta = \left(\frac{2}{3AR} \right)^{\frac{2}{3}} \left(\frac{8AR}{\pi^2} + \frac{2}{\pi} \right) \quad (11)$$

If rotation of the cylindrical particle in the z-direction (bed depth) is also taken into account, then the inclination angle θ is no longer equally probable, but follows a cosine probability distribution [19]. Now the θ -averaged projected area ratio $\overline{PA}_{ratio}(3D)$ becomes:

$$\overline{PA}_{ratio}(3D) = \frac{\int_0^{\pi/2} PA_{ratio}(\theta) \cos(\theta) d\theta}{\int_0^{\pi/2} \cos(\theta) d\theta} = \left(\frac{2}{3AR} \right)^{\frac{2}{3}} \left(AR + \frac{1}{2} \right) \quad (12)$$

In Table 2 Eqs. (11) and (12) are evaluated for the three aspect ratios considered. As seen, the angle-averaged projected area ratio is always greater than unity. This means that the drag force on cylindrical particles is higher compared to spherical particles if the cylindrical particles are allowed to rotate freely. Therefore, segregation is expected to cause cylindrical particles to rise to the top of the fluidized

Table 2

Angle-averaged projected area ratio's for cylinders of aspect ratio AR compared to a volume-equivalent sphere (see Eqs. (11), (12)).

	AR = 2	AR = 4	AR = 10
$\overline{PA}_{ratio}(2D)$	1.09	1.17	1.44
$\overline{PA}_{ratio}(3D)$	1.20	1.36	1.73

bed. Also segregation is expected to be more pronounced for higher aspect ratios.

We note that the above reasoning is not entirely exact, because the drag force coefficient C_d is in reality not constant, but 1.5 to 2.5 times higher (parallel and perpendicular to the flow) than that of a sphere [26–28]. Because this leads to an even larger drag force on the cylinders, the drawn conclusion will remain the same.

5. Results

5.1. Visual observations and regime maps

First, we studied the effect of varying mass fraction of cylindrical particles and superficial gas velocity on the fluidization behavior. Visual observations were used to construct a schematic regime map of these properties, which is shown in Fig. 7.

First the bed mobility was inspected. At low superficial gas velocities the bed is mostly static and no solids motion is observed. Upon increasing the gas velocity the bed turns into a dynamic state, where all particles can move freely through the bed, but no distinct bubbles are seen yet. Increasing the flow rate further causes bubble formation, which strongly promotes mixing.

For low fractions of the cylindrical particles bubble formation starts almost immediately upon increasing the gas flow. For higher fractions of cylindrical particles, there is a region in which the solids move but no bubbles are observed yet. As the bed contains a higher fraction of rods, the bed mobility at low velocities decreases. This is because the rod shaped particles have a tendency to entangle, keeping the bed in a rigid state. The spherical particles act as a sort of lubricant, their presence generally makes the bed behave more fluid-like.

The velocities for which segregation is observed are located in the 'dynamic' region (Fig. 7), where particles can move but no bubble

formation is observed. Here the non-spherical particles tend to sink to the bottom of the bed and/or align themselves with the walls of the setup. For segregation to set in, the particles must be able to move through the bed freely. At low velocities the bed is too static for this to occur. On the other hand; as the gas velocity is increased up to the point where bubbles form, mixing is strongly enhanced. This prevents segregation. The tendency to segregate also depends on the mass fraction of cylindrical particles. At low fractions, there are simply too few cylindrical particles to cluster; they are easily mixed. As more rods are present, clusters of cylindrical particles form more easily. For high fractions, the bed mobility goes down; which in turn also prevents particles from clustering. Therefore segregation was found to be most pronounced for beds containing 15–20% cylindrical particles. When >30% rod-shaped particles are present, no segregation is observed. Instead, there is an abrupt transition between a static and a vigorously bubbling bed.

For higher fractions of rods other interesting phenomena can be seen. In these mixtures channeling and bridging is observed. With channeling we mean that cylindrical particles align themselves with the flow direction to form channels that extend over the entire bed height (see Fig. 8d). For this to happen, a high fraction of cylindrical particles is required (see Fig. 7). For low rod fractions (<20%) channeling is less pronounced. Here, channels never extend longer than a few centimeters. As the velocity increases to $>1.6 \times U_{mf}^S$ the channels break down due to increased solids motion. Bridging means that the top of the bed is so rigid, that a dome-shaped cavity may form at the bottom of the bed, without the bed collapsing on top.

5.2. Pressure drop measurements

The pressure drop of the various mixtures of spherical and cylindrical particles was determined, starting from a fixed bed state. Upon increasing the superficial gas velocity, the pressure drop increases until the minimum fluidization velocity is reached. At this point the bed material is fully suspended by the gas flow, and the pressure drop typically becomes constant.

5.2.1. Steady state pressure drop profiles

In Fig. 9, the pressure drop profiles for mixtures of 0%, 20% and 40% cylindrical particles are shown as a function of the superficial gas velocity. For the 0% mixture (i.e. pure spheres) minimum fluidization

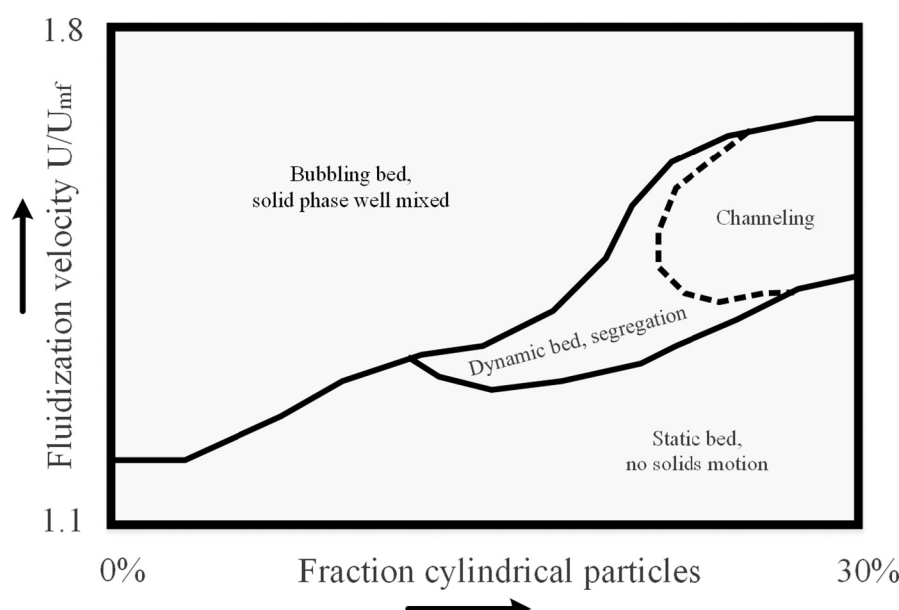


Fig. 7. Schematic regime map, showing the qualitative effects of superficial gas velocity and fraction of cylindrical particles on the fluidization behavior.

occurs at 3.1 m/s and the pressure drop at fluidization (28 mBar) is in good agreement with literature (29 mBar, see Cheng [29]).

Upon increasing the fraction of cylinders to 20%, a similar trend is found, but the minimum fluidization velocity has increased to 3.9 m/s. This result is quite remarkable. Based on our earlier analysis (see Section 4.2) one would expect elongated particles to experience a higher drag force, so U_{mf} is also expected to decrease accordingly. Instead we find that the elongated particles require a higher superficial velocity to initiate fluidization.

This result suggests that, aside from gravity and drag, there must be another mechanism at play. A plausible explanation can be found in an increase in particle-particle interaction, mostly through entanglement. Entangled particles actually act as if there are large agglomerates with a larger volume/mass that require a higher gas velocity to fluidize. Thus an agglomerate of elongated particles is experienced by the gas phase, as being –effectively– a larger, heavier particle.

When increasing the fraction of rod-shaped particles further, very different behavior is observed. For the 40% mixture, a minimum fluidization velocity can no longer be defined. Upon increasing the superficial gas velocity, there is no apparent motion of the particles. The bed remains static and induces a large pressure drop on the gas phase (almost 40 mBar). When a certain critical velocity is reached (around 4 m/s) the bed suddenly starts to fluidize, which can clearly be observed from the sharp decrease in pressure drop. After this point is reached, the particles start to reorganize, forming channels. This turns the bed into a fixed state again, which is indicated by another decrease in pressure till below ΔP_{mf} . Even at velocities that exceed 6 m/s, the bed weight is not fully supported by the gas, because the majority of the gas flow exits the bed through narrow channels, as shown in Fig. 8d.

The bed behavior can be further understood by inspecting the standard deviation of the pressure drop fluctuations, as indicated by the

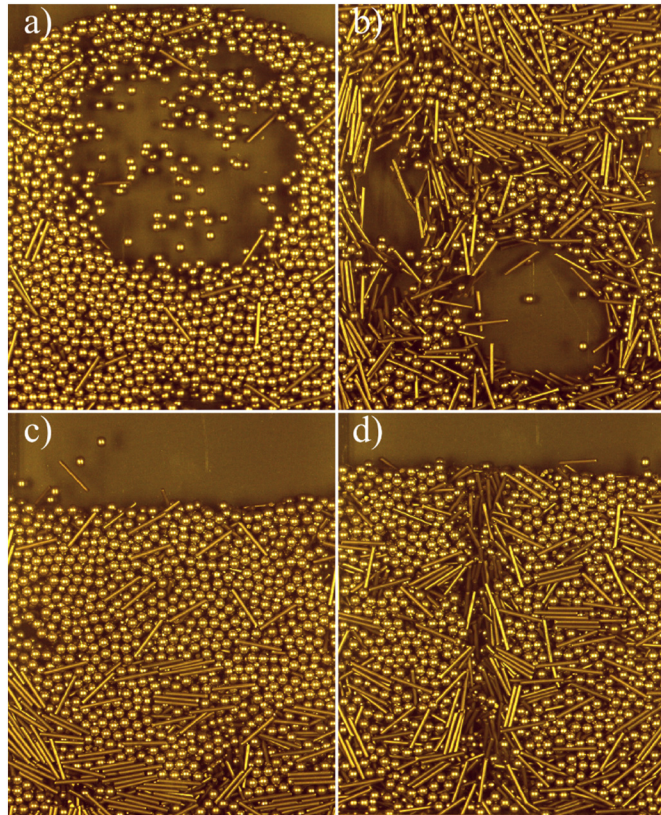


Fig. 8. Contrast enhanced images of the fluidized bed, showing different regimes for non-spherical particles. a) Bubbling bed at $f = 5\%$ and $U/U_{mf} = 1.2$, b) Bubbling bed at $f = 40\%$ and $U/U_{mf} = 2.0$, c) Segregating bed for $f = 20\%$ at $U/U_{mf} = 1.4$, d) Channeling phenomena for $f = 30\%$ at $U/U_{mf} = 1.5$.

green error bars in Fig. 9. For the more ‘ideal’ mixtures (0% and 20% rod-shaped particles) a sharp increase in the pressure drop fluctuations can be observed upon passing U_{mf} . This is primarily caused by formation of gas bubbles, which makes the bed material periodically move up and down in the bed. In a fixed bed state, the particles barely move and the pressure drop is fairly constant over time.

For the 40% mixture, quite a different behavior is observed. At a velocity of 4.1 m/s, the bed breaks free for a short moment, resulting in a sudden increase in pressure drop fluctuation. After some time, the material forms channels and settles again, which gives a low pressure drop fluctuation. It takes a very high velocity (>6 m/s) to reach the same degree of fluctuations that –for spheres– is already reached at 4 m/s.

These experiments indicate that the definition of ‘minimum fluidization’ becomes problematic for elongated particles. The fluidization of such particles is strongly subject to hysteresis: a single-point velocity at which (de)fluidization occurs no longer exists.

5.2.2. Frequency domain analysis

For completeness, the transient pressure signal was also analyzed in the frequency domain by a Fourier transformation (see Fig. 10). The main outcome is that for fluidized mixtures with a low fraction of rod-shaped particles (<20%), bubble motion can clearly be characterized by a sharp signal around 2 Hz (see Fig. 10a). This was confirmed visually, since it takes around 0.5 s for a bubble to pass the bed. For higher fluidization velocities, the frequency at which bubbles appear is slightly higher and more irregular, as can be seen by the lower and

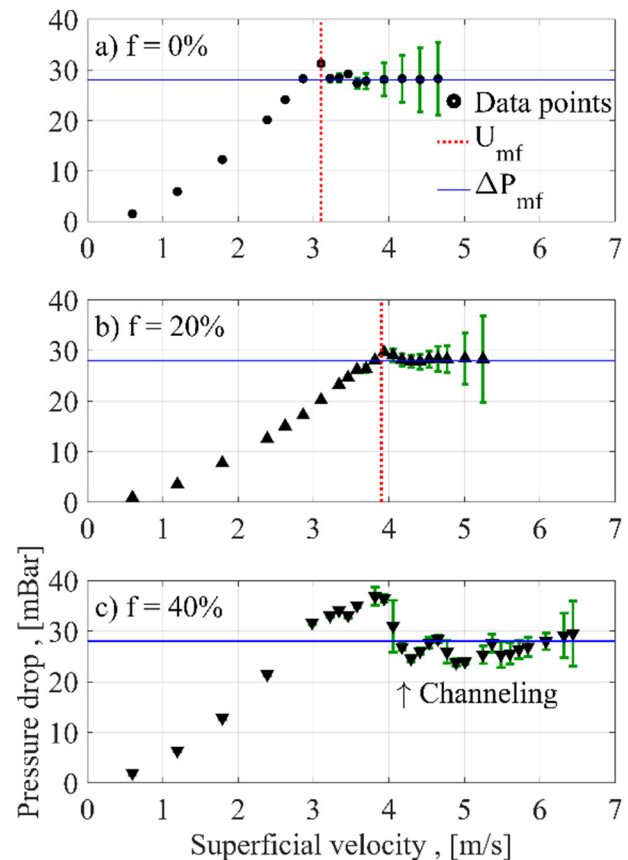


Fig. 9. Bed pressure drop versus superficial gas velocity, for a bed mass of 0.5 kg at different mass fractions of cylinders ($f = 0, 20$ and 40%). The red lines indicate the minimum fluidization velocity, the blue curves indicate the pressure drop at which fluidization is expected to occur (28 mBar). The green error bars show the standard deviation of the pressure drop, measured for each data point over a 30 s interval at a frequency of 10 Hz. For the 40% mixture, channel formation hinders full fluidization, indicated by the steep decrease in pressure drop around 4 m/s.

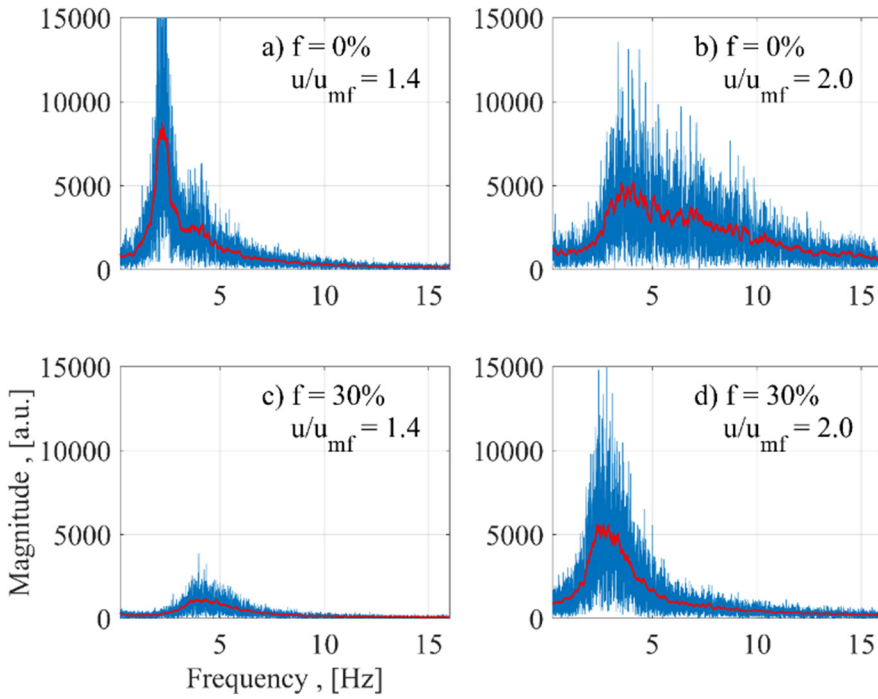


Fig. 10. Pressure drop frequency analysis using Fast Fourier Transforms, showing the amplitude spectrum. The blue curve represents the raw data, the red line is a smoothing spline function.

broader spectrum in Fig. 10b. The higher frequencies in the spectrum (5–15 Hz) seem to be more related to chaotic particle movement, rather than gross solid circulation patterns of bubble motion involving the entire bed. Visually the bed appears to be intensely fluidized.

For higher fractions of cylindrical particles, the bed is immobile at low velocities (compare Fig. 10a and c). Upon increasing the gas flow, one needs significantly higher fluidization velocities to reach the same level of bubbling compared to beds of only spheres (compare Fig. 10a and d). For the same velocity, the fluidization behavior is less vigorous (note the absence of signals exceeding 5 Hz in Fig. 9d). This can be

attributed to the rod-shaped particles, which intertwine and suppress the bed mobility.

5.3. Segregation experiments

In this section segregation experiments at constant composition and constant velocity are presented. The experiments are all started from a well-mixed state. Subsequently, the de-mixing of the solid phase is studied using the DIA technique introduced earlier.

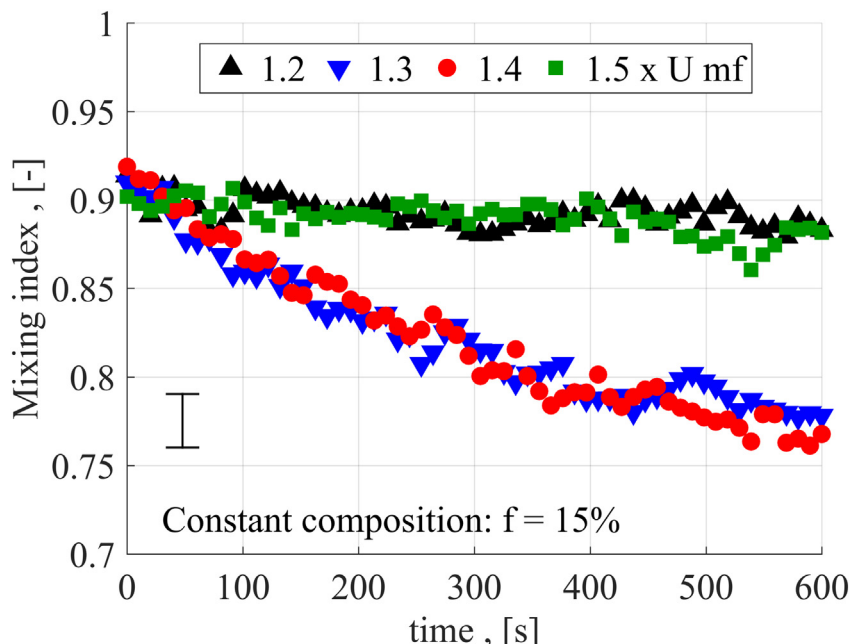


Fig. 11. Mixing index versus time, for a mixture of 15% cylindrical and 85% spherical particles at increasing fluidization velocity. The error bar on the bottom-left corner represents the standard deviation over each measurement point.

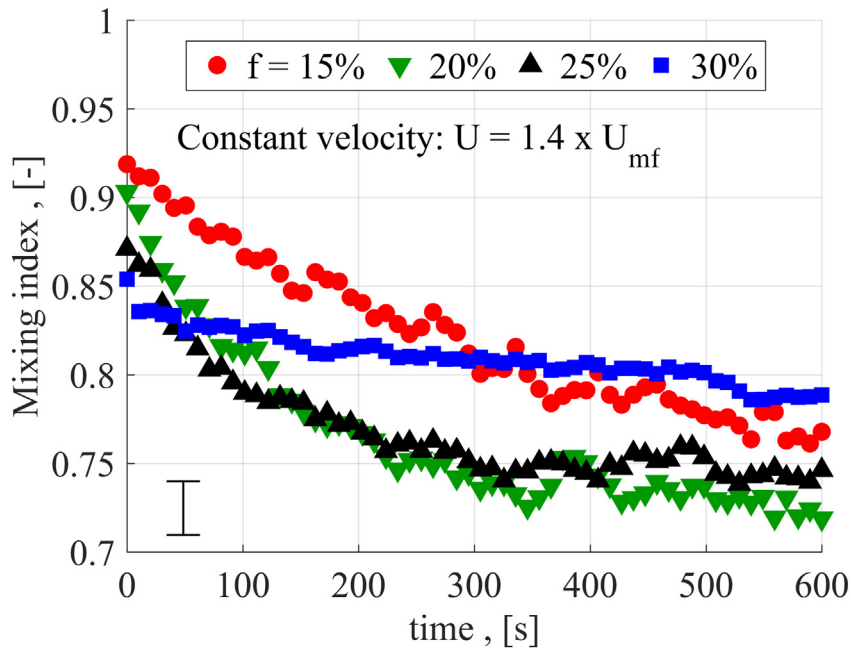


Fig. 12. Mixing index versus time, for mixtures of 15–30% cylindrical particles at constant fluidization velocity ($1.4 \times U_{mf}$).

5.3.1. Segregation at constant composition

Segregation experiments have been performed for a mixture at constant composition for different superficial gas velocities. For the DIA analysis the bed was recorded for a period of 10 min at a sampling frequency of 1 Hz. Before starting each experiment the bed was fluidized for several minutes at a high velocity (>6 m/s) to obtain a well-mixed state. Then the velocity was reduced to the desired value, and the recording was started.

Fig. 11 shows the mixing index versus time for mixtures containing 15% cylindrical particles for four different superficial gas velocities, which are all scaled by the minimum fluidization velocity of the spherical particles ($U_{mf}^S = 3.1$ m/s). Notice that the initial condition for all the experiments is at a mixing index of 0.9. The initial mixing index defers from unity because in practice a state of complete mixing cannot be obtained. Upon decreasing the superficial gas velocity starting from a well fluidized bed mutual alignment among rod-shaped particles instantly occurs.

As can be seen, at the lowest velocity (1.2 times minimum fluidization) the degree of mixing remains fairly constant over time. Here the bed is still static, preventing the occurrence of de-mixing. At the intermediate velocities (1.3–1.4 times U_{mf}) the bed is mobile enough to allow for segregation. Here the mixing index decreases to about 0.75. Segregation occurs mostly by entanglement of the cylindrical particles. The entanglement leads to the formation of intertwined particles that behave like large, heavy aggregates. These aggregates experience a lower effective drag force, causing them to sink to the bottom of the bed. Also strong alignment with the setup walls is observed. Upon increasing the velocity even more (1.5 times U_{mf}), mixing prevails. Here bubbles are formed and solids circulation patterns become visible. Consequently the bed remains well mixed.

5.3.2. Segregation at constant velocity

To investigate the effect of the rods fraction on segregation, several experiments were performed keeping the superficial gas velocity

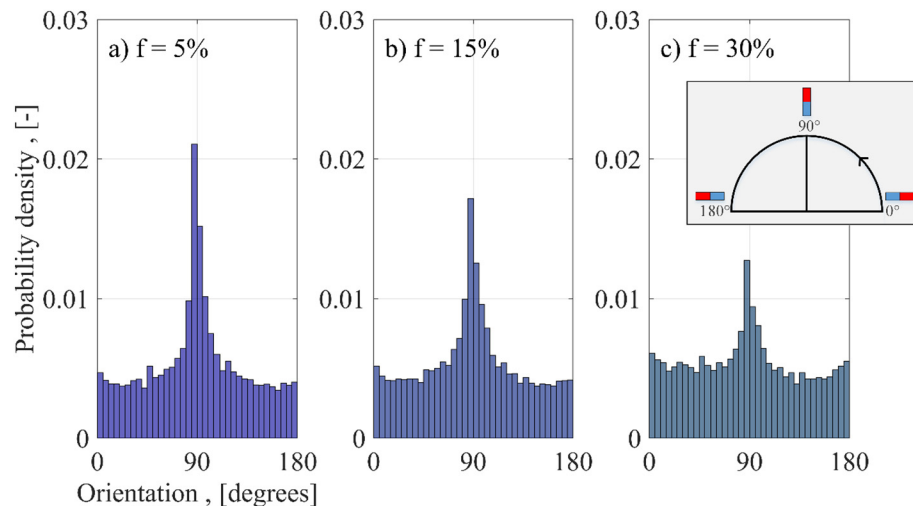


Fig. 13. Orientation of cylindrical particles in the fluidized bed at constant fluidization velocity ($U = 5.7$ m/s, $U/U_{mf} = 1.8$) for mixtures containing a) 5%, b) 15% and c) 30% cylindrical particles. Fig. 13c contains a small legend insert, which shows the particle's orientation at the axis limits.

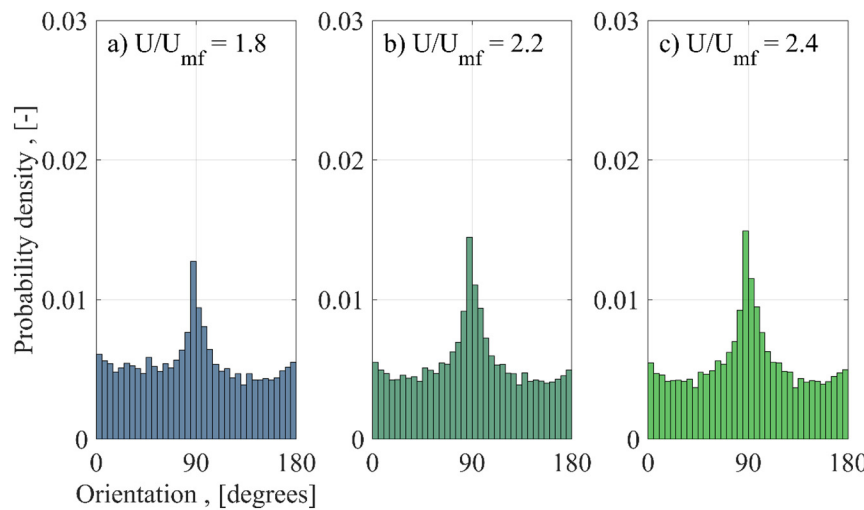


Fig. 14. Orientation distributions for mixtures containing 30% rod-shaped particles at different fluidization velocities: a) 1.8, b) 2.2, c) 2.4 times minimum fluidization velocity.

constant. The experimental procedure was the same as the one described in Section 5.3.1. The results are shown graphically in Fig. 12.

Notice that in this case, the initial mixing index is different for each experiment, because at increasing rod fractions it is increasingly more difficult to reach a well-mixed state, despite the relatively high gas velocity. Therefore, the initial mixing index (at $t = 0$) decreases with increasing fractions of cylindrical particles. The initial condition of the experiment is thus largely influenced by the bed composition.

When observing the trends in the graph, from 15% to 20% a considerable decrease in the mixing quality is observed. If more rod-shaped particles are present, the rods have an increasing tendency to cluster. This results in more segregation. The curves for the rod fractions of 20 and 25% appear quite similar, but the final mixing index for $f = 25\%$ is slightly higher. Also, we should bear in mind that the initial mixing index for 25% is already lower, which means that the difference between the initial and final state is significantly higher for $f = 20\%$.

The reason for this difference is that introducing more rods into the system reduces the bed mobility, which hinders de-mixing. The curve for $f = 30\%$ is almost flat. Because the bed is nearly immobile in this case, segregation cannot occur.

5.4. Orientation of particles in the fluidized bed

The orientation of the rod shaped particles in the fluidized bed could be determined from the recorded images using the method described in Section 3.2. First, we will discuss orientation distributions at constant velocity. The velocities used here are high, so that the bed remains well mixed. Next the composition is kept constant, showing the effect of the superficial velocity. Also spatial orientation differences within the bed are examined. Finally orientation distributions at lower velocities are shown; here the effect of segregation becomes visible.

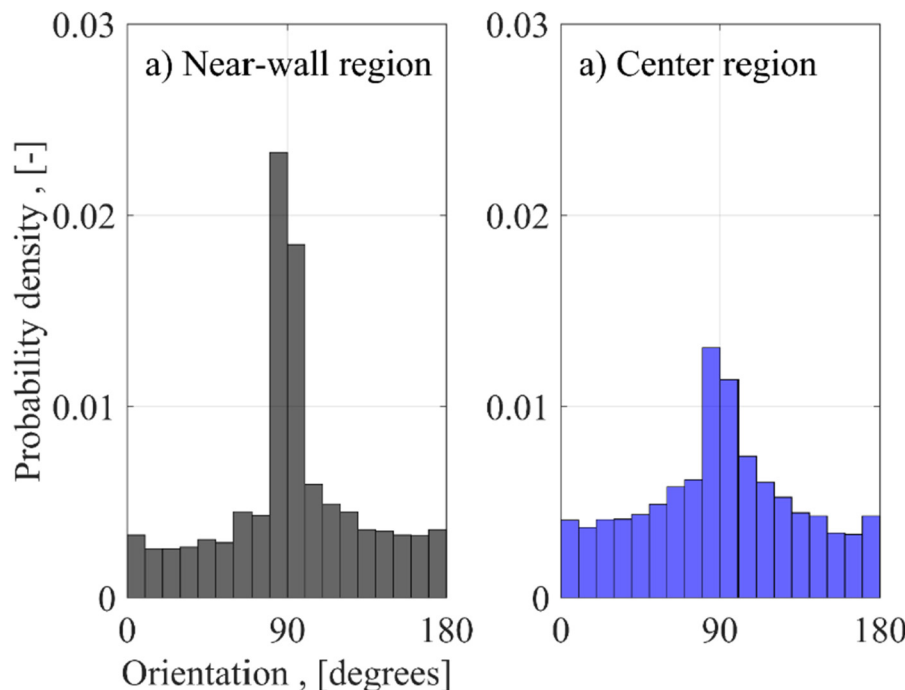


Fig. 15. Spatial orientation distributions within the fluidized bed, for a mixture of 5% cylinders at 2.2 times minimum fluidization. The total bed width is 100 mm, the center region extends from 33 to 66 mm, and the remaining parts are together defined as the near-wall region.

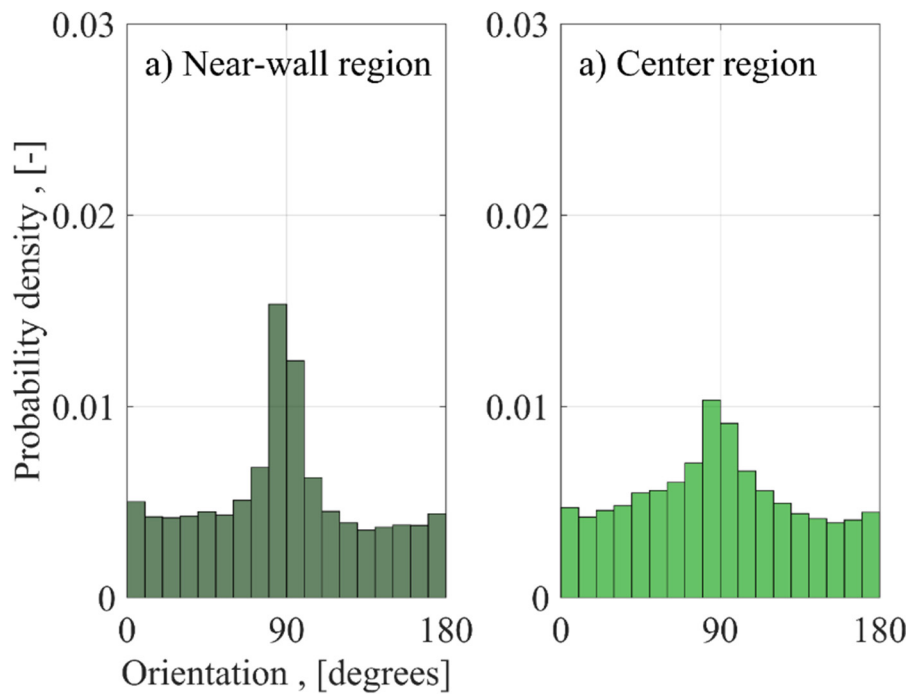


Fig. 16. Spatial orientation distributions within the fluidized bed, for a mixture of 30% cylinders at 2.2 times minimum fluidization.

In this section the particle orientation in the plane of measurement is expressed as the angle θ , where $\theta = 90^\circ$ corresponds to a vertical/standing position, whereas $\theta = 0$ or 180° corresponds to a horizontal position. The rotation proceeds counterclockwise, hence the origin lies in the right-half-plane. Because the DIA technique is 2-dimensional, the angle in the z-direction (bed depth) is not considered.

5.4.1. Orientation in bubbling fluidized beds at constant velocity

In Fig. 13 orientation distributions of cylindrical particles in a fluidized bed are shown. The data was extracted from ten time series of 600 images each, shot at 1 Hz; this yields a dataset of roughly 50.000 detected particles. A large population of particles is required to achieve good statistical averages. Note that in bubbling beds no segregation occurs, so that the fluidization process can be considered stationary. The distributions shown apply to the full bed, taking into account all grid cells (spatial distributions within the bed will be discussed later).

The bed is fluidized well above the minimum fluidization velocity, such that a gross solid circulation pattern was visible due to bubble motion. As can be seen in Fig. 13, in all cases the particles prefer to be in a vertical/standing position. Upon increasing the fraction of cylindrical particles in the bed, it is observed that the preferential orientation towards a vertical position decreases. To be able to explain these observations, it is instructive to look at the solids circulation pattern in the bed.

For low fractions of cylindrical particles, the bed material is still relatively free to move; this yields a mobile bed where large bubbles can be formed (for 5% cylinders the bubble diameter may extend up to 80% of the bed width). This, in turn, results in a relatively high solid fluxes downwards along the walls (i.e. the same mass of particles must flow through a smaller area per unit time). Because of the rapid down-flow of particles, there are strong solid shear forces due to collisions. This forces rod-shaped particles to attain a standing/vertical position. For a high fraction of rods, due to strong entanglement effects, no large bubbles are formed (for 30% cylinders the bubble diameter typically does not exceed 30% of the bed width). Here typically small bubbles at a higher frequency are found (as determined using Fourier analysis). The solids down-flux is therefore somewhat lower. In this case the particles are less strongly forced to a specific orientation.

5.4.2. Orientation in bubbling fluidized beds at constant composition

It was also investigated whether increasing the fluidization velocity at constant composition has any effect on the particle's orientation. For the range of velocities studied in this work, the effect of the velocity was found to be minor.

First for a bed of 5% and 15% cylinders the orientation distributions at 1.8, 2.0 and 2.4 m/s were determined: the orientation distributions were found to be almost identical. So, it seems that the fraction of rod-shaped particles has a much stronger effect on their orientation than the superficial gas velocity. The largest difference was found in the case of 30% rod-shaped particles, which is plotted in Fig. 14.

As can be seen, the higher gas velocity yields a slightly larger preference towards the vertical orientation. The reason for this is that increasing the velocity promotes bubbling action. When analyzing the images, it is clear visually that for the $2.4 \times U_{mf}$ case much larger bubbles are formed compared to the lower velocity ($1.8 \times U_{mf}$). Bigger

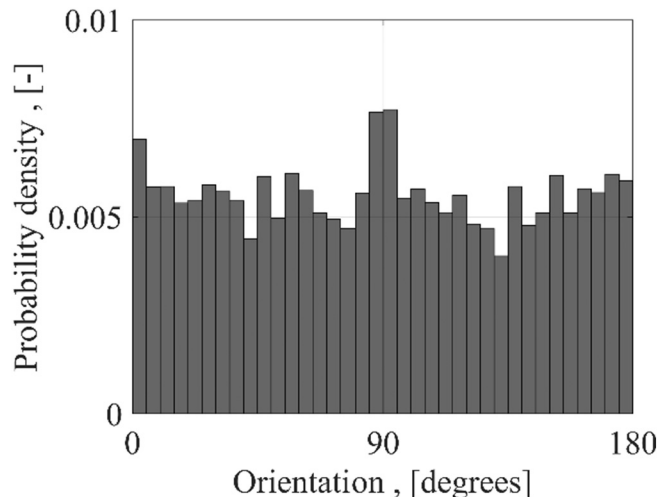


Fig. 17. Bed-averaged and time-averaged orientation distribution for a mixture of 20% spherical particles fluidized at 1.4 times the minimum fluidization velocity.

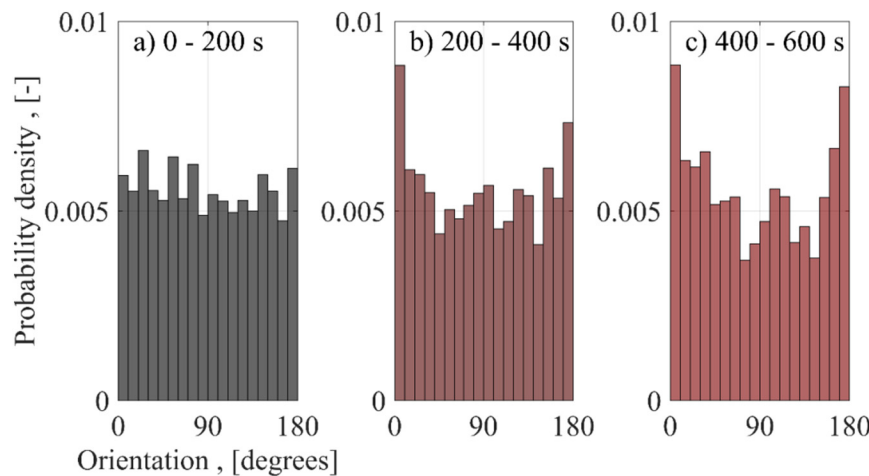


Fig. 18. Transient orientation distributions for the bottom-center section of a fluidized bed containing 20% spherical particles fluidized at 1.4 times minimum fluidization. The center-bottom region taken into consideration is 33 mm wide and 20 mm high.

bubbles force the particles to flow down at a higher flux. This introduces an axial shear on the rods, forcing them to align with the flow.

Note that all the experiments presented here are within the same regime (a bubbling fluidized bed), which yields similar solids circulation patterns irrespective of the specific velocity used. Because the main solids flow pattern is always the same, it is not strange that the particle orientation distribution is approximately constant.

5.4.3. Spatial orientation distributions within bubbling fluidized beds

Since the orientation of the cylindrical particles is carried out in grid cells, it also enables us to inspect spatial differences within the bed. As one may expect, strong differences between the wall and the bulk region can be observed. To illustrate this the bed is divided into three sections of 33 mm: a center region and two near wall regions. Next, the particle orientations in the center and near-wall regions are analyzed separately.

In Fig. 15 spatial orientation differences between center and near-wall regions are plotted for a 5% mixture at $2.2 \times U_{mf}$. In Fig. 16 the orientation distribution is plotted for a 30% mixture at the same gas velocity. As can be seen for the 5% case, a very strong vertical preference is found near the walls; for the 30% mixture the preferential orientation is much less. Notice that the distributions for both bulk regions are almost identical. This same trend is observed for all data sets (irrespective of gas velocity and/or composition). Probably the differences between mixtures at constant velocity (see Fig. 12) can be mainly explained by changes in the wall region. This indicates that bubble formation and the solids circulation flux are important factors affecting the particle orientation.

5.4.4. Orientation in non-bubbling fluidized beds

In non-bubbling fluidized beds, operated close to the minimum fluidization velocity, no gross solids circulation patterns occur. Therefore, the orientation of the cylindrical particles in such beds is expected to be more-or-less random. In Fig. 17 the orientation distribution for a non-bubbling bed is shown; as can be seen there is no significant preferential orientation. The particle orientation is similar to the expected value for a random distribution, which is $1/180 = 0.0056$.

On the other hand, non-bubbling beds are prone to segregation, where the cylindrical particles sink to the bottom of the bed (see Section 5.3). When particles sink they may attain a preferential horizontal position aligning with the bottom of the bed. Therefore in segregating systems one might expect that the orientation changes over time. In Fig. 18 the development of the orientation distribution over time is shown for a region near the bottom-center of a fluidized

bed. In this region particles accumulate over time due to segregation. The preferred orientation shifts slightly towards 0/180°, indicating that the particles align with the bottom wall.

Note that segregation phenomena are intrinsically chaotic, and the outcome of an experiment depends highly on the initial conditions (particle positions and orientations before starting the gas flow). Therefore, slightly different results are obtained upon each repetition, and the results shown in Fig. 18 should be considered as a qualitative result. Nonetheless these are instructive, since they are representative for the general behavior of the system.

6. Discussion and conclusions

For mixtures of spherical and cylindrical particles of equal mass, segregation occurs in the non-bubbling flow regime. For segregation to occur, the bed must be mobile, such that particles can move through the bed freely. At low fluidization velocities (1.2–1.5 times the minimum fluidization velocity) the fluidized bed is mobile and particles can move freely; here segregation is observed. If the velocity is increased up to the bubbling regime (velocity exceeding 1.7 times the minimum fluidization velocity), segregation diminishes due to bubble-induced mixing. In addition to the segregation phenomena, it was observed that rod-shaped particles can form organized structures that extend in size up to several particle lengths (e.g. channels).

Since the spherical and cylindrical particles have identical mass, the driving force for segregation must be explained by differences in drag and friction forces. The projected area of the cylindrical particles is smaller than that of the spheres, therefore theory predicts that segregation involves the rod-shaped particles floating to the top of the bed. Instead the experimental results show that the rods sink to the bottom; which differs from our initial expectations.

The proposed mechanism to explain this phenomenon is co-alignment. When two or three rod-shaped particles meet, they tend to align and aggregate due to mutual friction forces. These clustered aggregates are effectively larger, which decreases the drag force per unit mass, making them sink to the bottom of the bed. Therefore it seems that the concept of shape-driven segregation (which is the subject of this paper) is virtually non-existent, but rather size-driven segregation by clustering or aggregation of several particles occurs.

In the bubbling regime no segregation is observed. Here bubble induced mixing leads to solids circulation, keeping the bed well mixed. In the center of the bed there is net solids up flow; here the rod-shaped particles have no strong preferential orientation. Near the walls of the bed there is a net solids down flow; here strong alignment of the particle's orientation with the flow direction is observed.

The results presented in this work could act as a benchmark for numerical models that can handle fluidization of non-spherical particles.

List of symbols

Variable	Description	Units
AR	cylinder aspect ratio	—
k	grid cell index	—
A_{grid}	grid size	m^2
f	mass fraction cylindrical particles	kg/kg
r_{max}	maximum reflection count	m^{-2}
M	mixing index	—
$ rl $	normalized reflection count	—
N	number of grid cells	—
n	number of particles per cell	—
N_r	number of reflections	—
d	particle diameter	m
θ	particle orientation in xy-plane	degrees
ΔP	pressure drop	mBar
r	reflection count	m^{-2}
ε_{solid}^{2D}	solid area fraction	—
U	superficial gas velocity	m/s
t	time	s
S	variance	—
PA	projected area	m^2

Subscripts

Variable	Description
s	sphere
c	cylinder
mf	minimum fluidization

Acknowledgements

This research was funded by the European Research Council, under the Advanced Investigator Grant Scheme, contract no. 247298 (Multiscale flows), and the 3TU Centre of Excellence – Multiscale Phenomena.

References

- [1] A. Rao, J.S. Curtis, B.C. Hancock, C. Wassgren, Classifying the fluidization and segregation behavior of binary mixtures using particle size and density ratios, *AIChE J.* 57 (6) (2011) 1446–1458.
- [2] G.G. Joseph, J. Leboreiro, C.M. Hrenya, A.R. Stevens, Experimental segregation profiles in bubbling gas-fluidized beds, *AIChE J.* 53 (11) (2007) 2804–2813.
- [3] A. Marzocchella, P. Salatino, V. Di Pastena, L. Lirer, Transient fluidization and segregation of binary mixtures of particles, *AIChE J.* 46 (11) (2000) 2175–2182.
- [4] M.G. Rasul, V. Rudolph, M. Carsky, Segregation potential in binary gas fluidized beds, *Powder Technol.* 103 (2) (1999) 175–181.
- [5] P.N. Rowe, A.W. Nienow, A.J. Agbim, Preliminary quantitative study of particle segregation in gas fluidized-beds-binary-systems of near spherical particles, *Trans. Inst. Chem. Eng. Chem. Eng.* 50 (4) (1972) 324.
- [6] A.W. Nienow, P.N. Rowe, L.L. Cheung, A quantitative analysis of the mixing of two segregating powders of different density in a gas-fluidised bed, *Powder Technol.* 20 (1) (1978) 89–97.
- [7] A.W. Nienow, N.S. Naimer, T. Chiba, Studies of segregation/mixing in fluidised beds of different size particles, *Chem. Eng. Commun.* 62 (1–6) (1987) 53–66.
- [8] F. Garcia-Ochoa, A. Romero, J.C. Villar, A. Bello, A study of segregation in a gas-solid fluidized bed: particles of different density, *Powder Technol.* 58 (3) (1989) 169–174.
- [9] A.C. Hoffmann, L.P.B.M. Janssen, J. Prins, Particle segregation in fluidised binary mixtures, *Chem. Eng. Sci.* 48 (9) (1993) 1583–1592.
- [10] L. Huilin, H. Yurong, D. Gidaspow, Y. Lidan, Q. Yukun, Size segregation of binary mixture of solids in bubbling fluidized beds, *Powder Technol.* 134 (1) (2003) 86–97.
- [11] G. Olivieri, A. Marzocchella, P. Salatino, Segregation of fluidized binary mixtures of granular solids, *AIChE J.* 50 (12) (2004) 3095–3106.
- [12] F.P. Di Maio, A. Di Renzo, V. Vivacqua, A particle segregation model for gas-fluidization of binary mixtures, *Powder Technol.* 226 (2012) 180–188.
- [13] P.N. Ciesielski, M.F. Crowley, M.R. Nimlos, A.W. Sanders, G.M. Wiggins, D. Robichaud, B.S. Donohoe, T.D. Foust, Biomass particle models with realistic morphology and resolved microstructure for simulations of intraparticle transport phenomena, *Energy Fuel* 29 (1) (2014) 242–254.
- [14] R. Escudie, N. Epstein, J.R. Grace, H.T. Bi, Effect of particle shape on liquid-fluidized beds of binary (and ternary) solids mixtures: segregation vs. mixing, *Chem. Eng. Sci.* 61 (5) (2006) 1528–1539.
- [15] K. Vollmari, T. Oschmann, H. Kruggel-Emden, Mixing quality in mono-and bidisperse systems under the influence of particle shape: a numerical and experimental study, *Powder Technol.* 308 (2017) 101–113.
- [16] T. Oschmann, J. Hold, H. Kruggel-Emden, Numerical investigation of mixing and orientation of non-spherical particles in a model type fluidized bed, *Powder Technol.* 258 (2014) 304–323.
- [17] D.J. Parker, X. Fan, Positron emission particle tracking—application and labelling techniques, *Particology* 6 (1) (2008) 16–23.
- [18] J. Elfvingren, J. Kolehmainen, P. Saarenrinne, High performance particle tracking velocimetry for fluidized beds, *Computer Vision Theory and Applications (VISAPP)*, 2014 International Conference on, 3, IEEE 2014, January, pp. 441–449.
- [19] K.A. Buist, A.C. Gaag, N.G. Deen, J.A. Kuipers, Improved magnetic particle tracking technique in dense gas fluidized beds, *AIChE J.* 60 (9) (2014) 3133–3142.
- [20] K.A. Buist, T.W. van Erdewijk, N.G. Deen, J.A.M. Kuipers, Determination and comparison of rotational velocity in a pseudo 2-D fluidized bed using magnetic particle tracking and discrete particle modeling, *AIChE J.* 61 (10) (2015) 3198–3207.
- [21] O.O. Olaofo, K.A. Buist, N.G. Deen, M.A. van der Hoef, J.A.M. Kuipers, Segregation dynamics in dense polydisperse gas-fluidized beds, *Powder Technol.* 246 (2013) 695–706.
- [22] O.O. Olaofo, K.A. Buist, N.G. Deen, M.A. van der Hoef, J.A.M. Kuipers, Improved digital image analysis technique for the evaluation of segregation in pseudo-2D beds, *Powder Technol.* 244 (2013) 61–74.
- [23] VC, H. P. (1962). (U.S. Patent No. 3,069,654. Washington, DC: U.S. Patent and Trademark Office).
- [24] W. Godlieb, *High Pressure Fluidization* PhD Thesis Eindhoven University of Technology, 2011 2011.
- [25] P.M.C. Lacey, Developments in the theory of particle mixing, *J. Appl. Chem.* 4 (5) (1954) 257–268.
- [26] R. Von Mises, *Theory of Flight*, Dover Books on Aeronautical Engineering Series, , Dover Publications, 1959.
- [27] A. Vakil, S.I. Green, Drag and lift coefficients of inclined finite circular cylinders at moderate Reynolds numbers, *Comput. Fluids* 38 (9) (2009) 1771–1781.
- [28] M.C. Hoang, A. Laneville, F. Légeron, Experimental study on aerodynamic coefficients of yawed cylinders, *J. Fluids Struct.* 54 (2015) 597–611.
- [29] N.S. Cheng, Wall effect on pressure drop in packed beds, *Powder Technol.* 210 (3) (2011) 261–266.